Engineering Structures 353 (2026) 122253

Contents lists available at ScienceDirect

Engineering Structures

journal homepage: www.elsevier.com/locate/engstruct

Restoration of fire-damaged high-performance concrete columns by post-fire water-CO_2 cyclic curing

Hangqi Lou [a], Tiejun Liu [a], Dujian Zou [a], Ye Li [b,*]

[a] Guangdong Provincial Key Laboratory of Intelligent and Resilient Structures for Civil Engineering, Shenzhen 518055, China
[b] Department of Civil, Maritime and Environmental Engineering, University of Southampton, Southampton SO17 1BJ, UK

ARTICLE INFO

Keywords:
High performance concrete column
Fire exposure
Post-fire curing
Microstructural changes
Mechanical performance

ABSTRACT

This study experimentally investigates the post-fire mechanical performance and recovery potential of high-performance concrete (HPC) columns exposed to standard fire conditions followed by water-CO_2 cyclic re-curing. The columns were subjected to one hour of heating according to the ISO 834 standard fire curve and subsequently re-cured for 30 days. A comprehensive evaluation was performed, including internal temperature profiling, surface damage observation, microstructural analysis, load-displacement response, and failure mode characterization. Results show that HPC columns with a lower water-to-binder ratio (W/B) suffered more severe internal damage due to higher peak temperatures and steeper thermal gradients. Consequently, their residual load-bearing capacity was more significantly reduced than that of columns with a higher W/B. The conventional 500 °C isotherm method effectively predicted the post-fire capacity of high-W/B columns but overestimated that of low-W/B columns, for which a 400 °C threshold provided a better approximation. Water-CO_2 cyclic re-curing markedly enhanced the mechanical recovery of fire-damaged columns by promoting rehydration and carbonation reactions, which filled coarsened pores, healed microcracks, and partially sealed macrocracks, thereby restoring structural integrity. After re-curing, the load-bearing capacities of the low- and high-W/B columns recovered to 67.3 % and 100.9 % of their original values, respectively.

1. Introduction

High-performance concrete (HPC) is increasingly used in modern construction due to its high compressive strength, low permeability, and exceptional durability. However, when exposed to fire, HPC members are prone to severe surface cracking, internal degradation, and even explosive spalling, all of which substantially compromise structural integrity and serviceability. Conventional post-fire repair methods, such as section enlargement or shotcrete overlay, are often labor-intensive, costly, and unsuitable for large-scale rehabilitation of structural components [1–4]. Therefore, understanding the residual performance of HPC columns after fire exposure and developing efficient recovery techniques are critical to ensuring the safety and functionality of fire-affected infrastructure.

Extensive research has examined the fire behavior and residual strength of normal-strength concrete (NSC) and high-strength concrete (HSC) columns [5–7]. The risk of explosive spalling in HSC has been mitigated by incorporating polypropylene (PP) fibers, which facilitate vapor pressure relief during heating [8–11]. Kodur et al. [5,12,13] proposed simplified models for predicting the residual load-bearing capacity of NSC and HSC members after fire exposure. However, the thermal response of HPC differs substantially from that of NSC and HSC because of its dense microstructure, inclusion of pozzolanic materials, and the predominance of siliceous aggregates. Between 200 and 400 °C, HPC may even exhibit slight strength gains due to continued hydration of unreacted cement, secondary pozzolanic reactions, and the formation of crystalline phases such as tobermorite ($C_5S_6H_5$) and xonotlite (C_6S_6H) [14–17]. The high thermal expansion of siliceous aggregates relative to calcareous aggregates increases the risk of thermal cracking [18,19]. In addition, compared with conventional concrete containing coarse aggregates, HPC designed based on optimized particle packing may exhibit lower permeability at elevated temperatures due to the absence of coarse aggregates [7,8,20,21]. Consequently, residual capacity models developed for NSC or HSC cannot be directly applied to HPC without modification.

Most existing studies attribute post-fire strength reduction of concrete primarily to the deterioration of material properties at elevated temperatures, such as dehydration, decomposition of hydration

* Corresponding author.
E-mail addresses: 25B354004@stu.hit.edu.cn (H. Lou), liutiejun@hit.edu.cn (T. Liu), zoudujian@163.com (D. Zou), ye.li@soton.ac.uk (Y. Li).

https://doi.org/10.1016/j.engstruct.2026.122253
Received 16 November 2025; Received in revised form 6 January 2026; Accepted 26 January 2026
Available online 30 January 2026

products, and microcracking at the paste or mortar scale [5,22,23]. While these mechanisms are well documented, they do not fully capture the behavior of fire-exposed reinforced concrete columns, in which damage development extends beyond the material scale. Pronounced thermal gradients during heating and cooling induce restrained thermal deformation and tensile stresses at the member level, leading to the initiation and propagation of macro-scale cracks. These structural-scale cracks can significantly compromise stiffness, confinement effectiveness, and global load-bearing performance, even when a substantial portion of the material-level compressive strength is retained [24–26]. Despite their importance, the interaction between material degradation and structural-scale damage evolution in fire-damaged HPC columns remains insufficiently understood.

In parallel, recent research has demonstrated that post-fire self-healing and re-curing techniques can promote rehydration of thermally decomposed phases and seal fire-induced cracks, resulting in partial recovery of mechanical properties [27–40]. Among these methods, water-CO_2 cyclic re-curing has shown particular promise by alternately activating hydration and carbonation reactions, generating healing products that densify the cement matrix and fill microcracks [41,42]. Due to the high content of unhydrated cement and reactive supplementary materials, HPC exhibits enhanced chemical reactivity and a greater potential for microstructural recovery compared with conventional concretes [42–47]. However, the overwhelming majority of existing studies remain confined to paste, mortar, or small-scale specimens, where structural constraints, non-uniform temperature histories, and load-transfer mechanisms are not represented.

Accordingly, the effectiveness of post-fire re-curing strategies at the level of full structural members, where material degradation, macro-scale cracking, and global stability interact, remains largely unexplored. This study directly addresses this gap by investigating the post-fire degradation and recovery behavior of reinforced HPC columns at the structural scale. Columns were subjected to ISO 834 standard fire exposure followed by water-CO_2 cyclic re-curing, allowing explicit coupling of non-uniform temperature histories, depth-dependent damage characteristics, and axial load-bearing performance. Two water-to-binder ratios (W/B = 0.18 and 0.36) were examined to capture the influence of matrix density and thermal sensitivity. By integrating internal temperature monitoring, microstructural characterization, and axial compression testing, this work elucidates how material-scale recovery mechanisms translate, or fail to translate, into structural-level strength and stiffness restoration. The findings provide mechanistic insight and practical guidance for post-fire assessment and repair of fire-damaged high-performance concrete structural elements.

2. Experimental program

2.1. Concrete mix design

The mix proportions of all specimens are listed in Table 1. The HPC mixtures were prepared using CEM I 52.5 Portland cement, fine aggregates, silica flour, silica fume (SF), superplasticizer, water, and polypropylene (PP) fibers. To examine the influence of mixture strength on post-fire performance, two W/B of 0.18 and 0.36 were adopted, designated as the low-water (LW) and high-water (HW) mixtures, respectively. Pheoplus 325 R superplasticizer was used to ensure adequate flowability. The particle size ranges of silica flour and sieved quartz sand were 15–293 μm and 0.08–1.18 mm, respectively. The particle size distribution curves of cement, SF, silica flour, and sand are shown in Fig. 1, and the corresponding D10, D50, and D90 values are summarized in Table 2. Monofilament cylindrical PP fibers (length = 12 mm, diameter = 30 μm) were incorporated at 4.5 kg/m^3 to prevent explosive spalling during fire exposure.

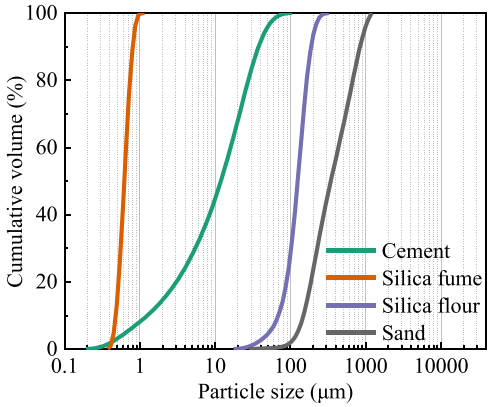

Fig. 1. Particle size distribution curves of cement, silica fume, silica flour and sand.

Mixing was performed in an 80 L planetary mixer. Dry constituents (cement, silica fume, fine aggregates, and silica flour) were blended for 6 min to ensure uniform dispersion. The premixed solution of water and superplasticizer was then added, followed by an additional 4 min of mixing until a homogeneous mix was achieved. PP fibers were introduced gradually over 1 min, and mixing continued for 3 min to ensure uniform fiber distribution. Fresh mixtures were cast horizontally into column molds, covered with plastic sheets for 24 h, demolded, and water-cured at 20 ± 3 °C for 14 days, followed by 75 days of air storage under laboratory conditions. Under identical curing, 150 mm cubes were tested for compressive strength at room temperature, yielding 104.4 MPa for the LW mix and 53.1 MPa for the HW mix.

2.2. Column design and test set-up

Six short reinforced HPC columns (200 mm × 200 mm × 600 mm) were fabricated using the two mix designs. The specimen identifiers and treatment conditions are summarized in Table 3. The letters A, H, and C represent ambient-cured, fire-damaged, and water-CO_2 re-cured specimens, respectively.

Each column contained four 12 mm-diameter hot-rolled steel bars as longitudinal reinforcement, enclosed by 6 mm-diameter stirrups spaced at 80 mm. Three additional stirrups were concentrated at each end to prevent premature end failure. The nominal concrete cover was 20 mm. Four thermocouples (TC1-TC4) were embedded at mid-height: TC1-TC3 were located at depths of 20 mm, 60 mm, and 100 mm from the surface, while TC4 was attached to a longitudinal steel bar (Fig. 2).

Table 2
The particle size distribution of the materials (μm).

Materials	D10	D50	D90
Cement	1.26	11.91	37.81
Silica fume	0.48	0.62	0.80
Silica flour	58.05	112.51	170.71
Sand	148.85	343.72	842.42

Table 1
Mix proportions of concrete (kg/m^3).

Mix design	Cement	Fine aggregates	Silica flour	Silica fume	Superplasticizer	Water	Polypropylene fibers
LW	929.9	874.1	288.3	93.0	30.7	184.1	4.5
HW	872.4	820.1	270.5	87.2	6.1	345.5	4.5

Table 3
Specimen identifiers and treatment conditions.

Series	Specimen ID	Treatment
A	LW-A HW-A	Ambient curing
H	LW-H HW-H	ISO 834 standard fire exposure (1 h)
C	LW-C HW-C	Fire damage + 30 days of re-curing

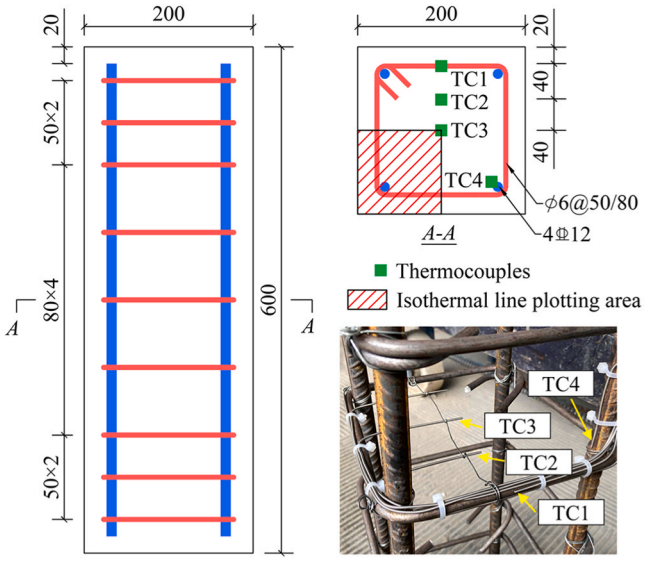

Fig. 2. Column reinforcement details and thermocouple layout (dimensions in mm).

To minimize friction-induced damage during axial loading, both column ends were coated with Sikadur-330 CN epoxy and wrapped with 10 cm-wide carbon-fiber-reinforced-polymer (CFRP) strips. A thin plaster layer was applied to ensure uniform contact with the loading plates. The load-testing setup is shown in Fig. 3. Axial deformation was measured over a 250 mm segment centered at mid-height using linear variable displacement transducers (LVDTs) mounted on steel holders. Strain gauges (120 Ω, 50 mm gauge length) were installed at the midpoints of all four column faces to capture axial and lateral strains. Columns were tested under axial compression using a 3000 ton-capacity testing machine at a constant displacement rate of 0.2 mm/min until failure. All measurements (load, displacement, and strain) were synchronized through a TDS-530 data acquisition system.

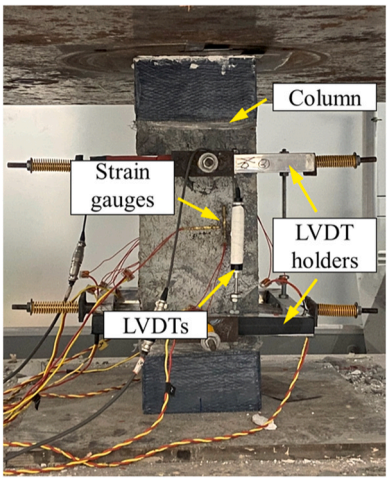

Fig. 3. Axial load-bearing capacity test setup.

2.3. Heating and re-curing procedure

Columns in Series H and C were heated in a gas furnace following the ISO 834 standard fire curve for 60 min (Fig. 4a). After heating, specimens were left to cool naturally inside the furnace. Temperatures were logged every 10 s through the embedded thermocouples to capture both internal and furnace temperature histories (Fig. 4b).

Once cooled to room temperature, the C-series columns were subjected to 30 days of water-CO_2 cyclic re-curing. Each cycle consisted of 3 days of immersion in lime-saturated water, followed by 3 days of carbonation exposure. During the immersion stage, specimens were fully submerged to promote rehydration of thermally decomposed hydration products. After immersion, surface water was removed before transferring the specimens to the carbonation chamber. The carbonation stage was conducted at 30 ± 1 °C, 40 ± 1 % relative humidity, and 20 ± 0.2 % CO_2 concentration. This relatively low humidity level was selected to facilitate CO_2 diffusion into the pore structure while avoiding pore saturation caused by the preceding immersion stage, thereby promoting efficient carbonation reactions. The adopted curing parameters and cycle duration were selected in accordance with recommendations from previous studies [41,42].

2.4. Microstructure observation

To assess fire-induced deterioration and the effects of re-curing at various depths, core samples were extracted from each column. The cores were sectioned at 10 mm intervals and examined using a Phenom ProX G6 scanning electron microscope (SEM) equipped with a backscattered electron (BSE) detector.

Sample preparation involved soaking in isopropanol for 24 h to arrest ongoing hydration and carbonation, followed by vacuum drying at 60 °C for 24 h. The samples were then embedded in epoxy resin and allowed to cure. Sequential polishing was performed with 600, 1200, and 2000-grit sandpapers, followed by fine polishing with 3 μm and 1 μm diamond pastes on a BUEHLER TexMet P cloth under 20 N load for 20 min each. Gold sputtering was applied to enhance conductivity before imaging. All BSE images were captured at an acceleration voltage of 15 kV.

3. Results

3.1. Temperature profile

The temperature profiles recorded by embedded thermocouples during fire exposure are presented Fig. 5. As expected, the rate of temperature increase decreased with greater embedment depth. Thermocouples TC2 and TC3 exhibited temporary plateaus at approximately 120–130 °C, corresponding to the latent heat consumed during the vaporization of pore water. The vaporization temperature exceeded 100 °C because of high capillary pressure in fine pores and the complex liquid-vapor-air interface within the matrix [48].

In the LW-H column, a second plateau was observed around 200 °C in TC2 and TC3, attributed to steam release resulting from the expansion and melting of PP fibers [20,49,50]. This phenomenon was less evident in the HW-H column because the internal temperatures of TC2 and TC3 remained below 200 °C.

The peak internal temperatures in both LW-H and HW-H columns occurred after furnace shutdown. This delayed response resulted from inward heat transfer from the hot exterior to the cooler core. Thermocouple TC4, attached to the longitudinal reinforcement, exhibited a trajectory similar to TC1 (20 mm depth), indicating significant heating of the reinforcement zone. The denser microstructure and lower porosity of the LW-H mixture led to higher thermal conductivity and lower

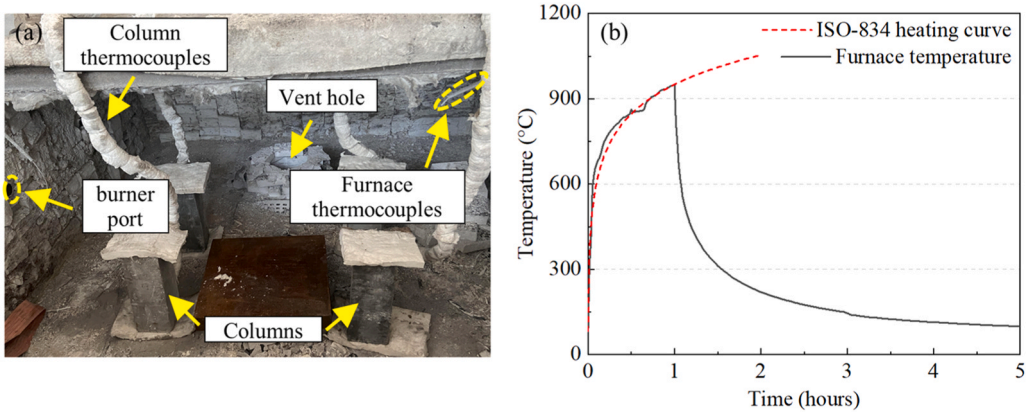

Fig. 4. (a) Heating of columns in a gas furnace and (b) temperature history during fire exposure.

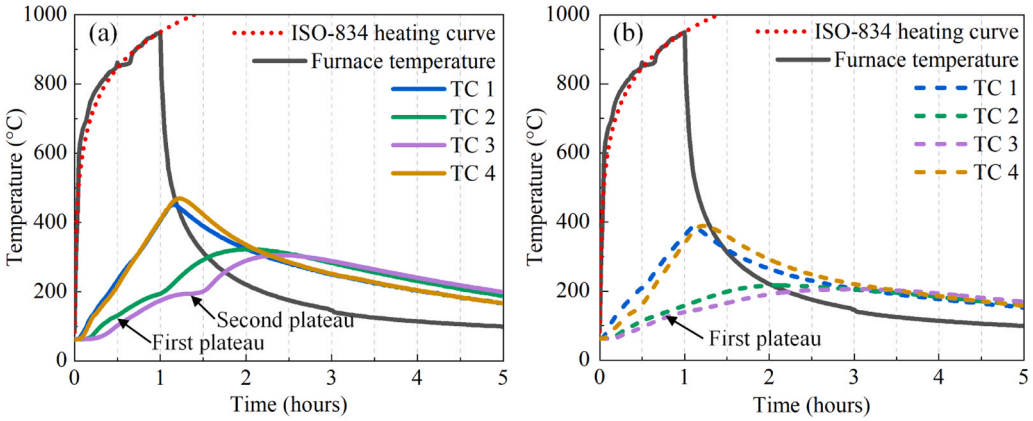

Fig. 5. Temperature histories during fire exposure: (a) LW-H; (b) HW-H.

specific heat capacity than the HW-H mixture [6,13,51], resulting in greater thermal diffusivity and faster heat penetration. Thermal diffusivity, α, is defined as:

$$\alpha = \frac{\lambda}{\rho c} \tag{1}$$

where λ is the thermal conductivity, ρ is the density, and c is the specific heat capacity.

The higher α of the LW-H column promoted deeper heat transfer and higher internal temperatures, leading to greater microstructural damage. At elevated temperatures, dehydration and decomposition of cement hydration products, combined with thermal expansion mismatches between paste and aggregate, lead to degradation in mechanical performance. Prior studies [41,42,52,53] have shown that microcracking in HPC typically initiates above 400 °C, with cracks exceeding 1 μm becoming a key driver of mechanical degradation.

Fig. 6 shows the temperature differences between thermocouple pairs, derived by subtracting the reading of a shallower thermocouple from that of a deeper one. A positive value indicates a downward (outward-hotter) temperature gradient, while a negative value indicates surface cooling. Steep thermal gradients induce tensile stress in cooler internal regions due to restrained thermal expansion [54], potentially leading to temperature-gradient-induced cracking [55]. Fu [26]

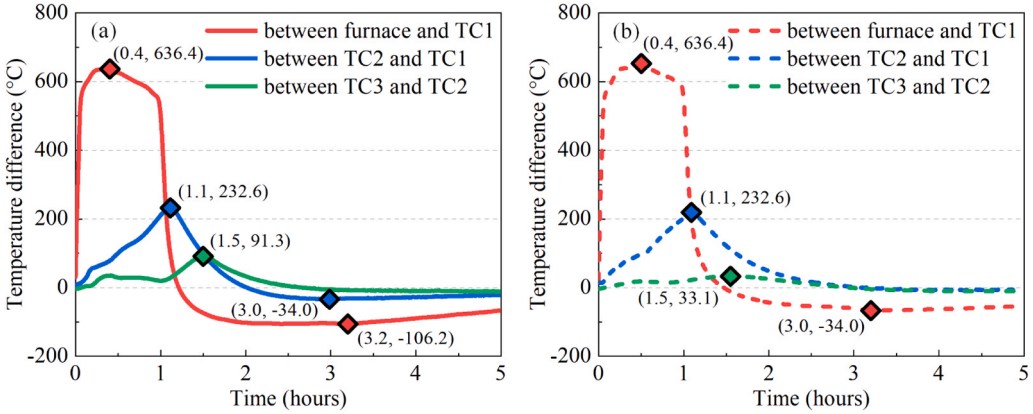

Fig. 6. Temperature differences between thermocouples: (a) LW-H, (b) HW-H.

reported cracking in a 25 mm-thick mortar specimen when the temperature difference reached 45 °C (1.8 °C/mm).

In the present study, the LW-H column exhibited higher internal gradients. The maximum temperature difference between TC2 and TC1 (20–60 mm) reached 232.6 °C (≈5.8 °C/mm), and between TC3 and TC2 (60–100 mm) reached 91.3 °C (≈2.3 °C/mm), both exceeding Fu's cracking threshold. By contrast, the HW-H column displayed a much smaller gradient (33.1 °C, ≈0.8 °C /mm) in the same region, indicating a lower risk of deep cracking. During cooling, rapid surface temperature drops produced negative gradients, promoting surface tensile stresses and further crack propagation.

In addition to cracking induced by internal thermal mismatch and temperature gradients within the concrete, differential thermal expansion between steel reinforcement and the surrounding concrete may generate localized tensile cracking near the reinforcement. However, the high-performance concrete (HPC) used in this study incorporated siliceous aggregates with relatively high coefficients of thermal expansion, thereby reducing the mismatch with steel reinforcement [54]. Furthermore, the peak temperatures measured in the reinforcement were 469.6 °C and 388.5 °C for the LW-H and HW-H columns, respectively, which are below temperature ranges typically associated with significant reinforcement-induced cracking [56,57]. Given the shallow embedment depth of the reinforcement (20 mm), any such cracking is expected to be confined to near-surface regions. Consequently, its contribution to global stiffness degradation and load-bearing capacity is substantially smaller than that of cracking driven by steep temperature gradients within the concrete. The observed cracking behavior and post-fire structural degradation in this study are therefore considered to be governed predominantly by concrete-related thermal effects rather than by reinforcement-induced thermal expansion.

The thermocouple measurements obtained after 1 h of heating were fitted along the column depth to derive the temperature-depth profiles shown in Fig. 7. From these fitted curves, the surface peak temperatures were determined to be 847.5 °C and 879.2 °C for the LW-H and HW-H columns, respectively. These values are consistent with prior reports [58–62], which indicated that surface temperatures typically reach approximately 800–900 °C after one hour of ISO 834 fire exposure. The maximum temperatures recorded by the embedded thermocouples are listed in Table 4. Based on these measurements and assuming symmetric four-side heating, the temperature field across the column cross-section was obtained through linear interpolation [22,63] (Fig. 8). The resulting isotherm depths were subsequently used to evaluate material degradation and estimate residual strength.

3.2. Visual inspection of the columns

The post-fire surface conditions are shown in Fig. 9. The LW-H column developed a grid-like cracking pattern with relatively wide cracks, while the HW-H column exhibited finer and denser surface cracks.

Two dominant mechanisms contributed to surface cracking: (1) temperature-gradient-induced cracking occurred during cooling, as rapid surface cooling produced tensile stress in the exterior layer; (2) high-temperature shrinkage arose at later stages of heating, when dehydration of C-S-H caused contraction of the paste, whereas quartz aggregates continued expanding [7,64–67]. Consequently, shrinkage-induced cracking typically initiated near 700–800 °C and was confined to a shallow zone (~5 mm in this study). The finer crack network on the HW-H surface was associated with its higher W/B ratio and larger amount of hydration products, which led to greater thermal shrinkage but lower intrinsic strength [68,69].

Although temperature-gradient-induced cracking that developed within the columns during heating could not be observed directly through surface inspection, the temperature differential analysis in Section 3.1 clearly indicates that such cracking was inevitable in both specimens. In the LW-H column, the much steeper internal gradients generated high transient thermal stresses, especially near the interface between the heated outer layer and the relatively cooler core. The differential expansion constrained by the cooler interior would have induced biaxial tensile stresses perpendicular to the heat flow, initiating crack networks that propagated inward as heating progressed. These internal macrocracks not only disrupted the continuity of the load path but also degraded the bond between longitudinal reinforcement and

Table 4
Maximum temperatures recorded by embedded thermocouples.

Specimen ID	Maximum temperatures (°C)			
	TC1	TC2	TC3	TC4
LW-H	451.6	322.8	305.5	469.6
HW-H	386.0	216.7	205.8	388.5

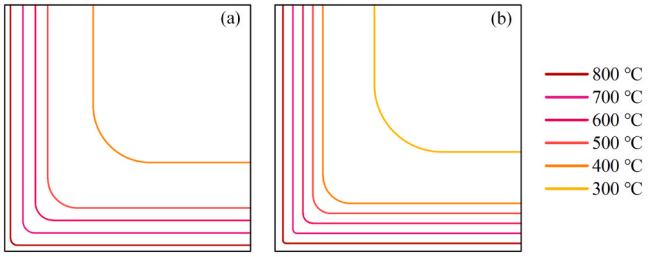

Fig. 8. Estimated temperature distribution across the column cross-section: (a) LW-H; (b) HW-H.

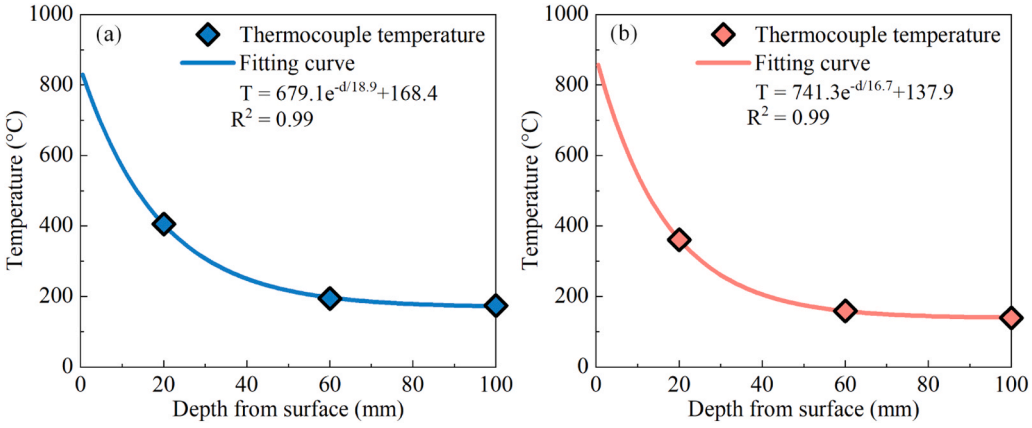

Fig. 7. Fitted temperature-depth profiles after 1 h of fire exposure: (a) LW-H, (b) HW-H.

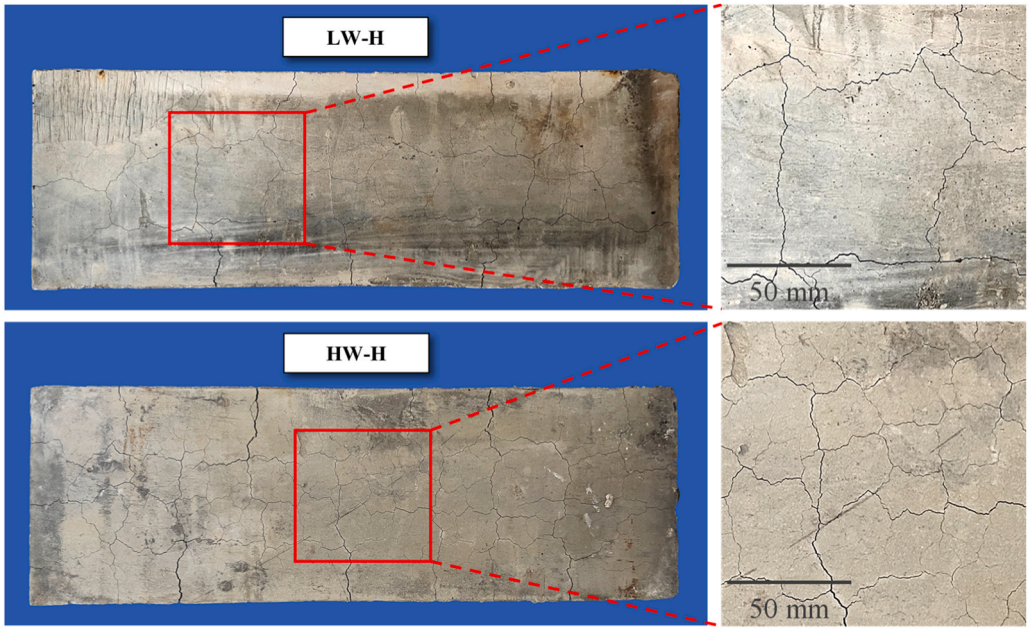

Fig. 9. Surface appearance of columns after fire exposure.

surrounding concrete. Furthermore, they reduced the confinement of the core concrete, amplifying lateral dilation and accelerating strength loss during loading. The detailed influence of these thermally induced cracks on axial load transfer and structural integrity is examined in Section 4.

After 30 days of water-CO_2 cyclic re-curing, substantial surface changes were observed on both columns (Fig. 10). Numerous white crystalline deposits filled or bridged surface cracks, indicating active rehydration and carbonation occurring during the restoration of fire-damaged concrete. The magnified images revealed that narrow cracks were nearly completely sealed, while wider ones were only partially filled, suggesting that the precipitation and recrystallization processes were insufficient to bridge the larger voids. Consequently, these unfilled regions acted as weak zones, potentially limit full restoration of the column's load-bearing capacity.

3.3. Changes of microstructure

Back-scattered electron (BSE) images of the concrete microstructure at various depths in the LW-H and HW-H columns are shown in Fig. 11 and Fig. 12, respectively. In both cases, the density and width of microcracks decreased progressively with depth. These cracks, classified as microcracks, originated from the thermal decomposition of hydration products and the mismatch in thermal expansion between paste and aggregate. They are distinct from the macrocracks discussed in Section 3.2, which were primarily induced by steep temperature gradients. In the present study, microcrack dimensions were not quantitatively measured; therefore, the microstructural discussion is based on qualitative comparison and its consistency with established temperature–damage relationships. The observed depth-dependent cracking trend correlates closely with the peak temperatures at each depth, estimated

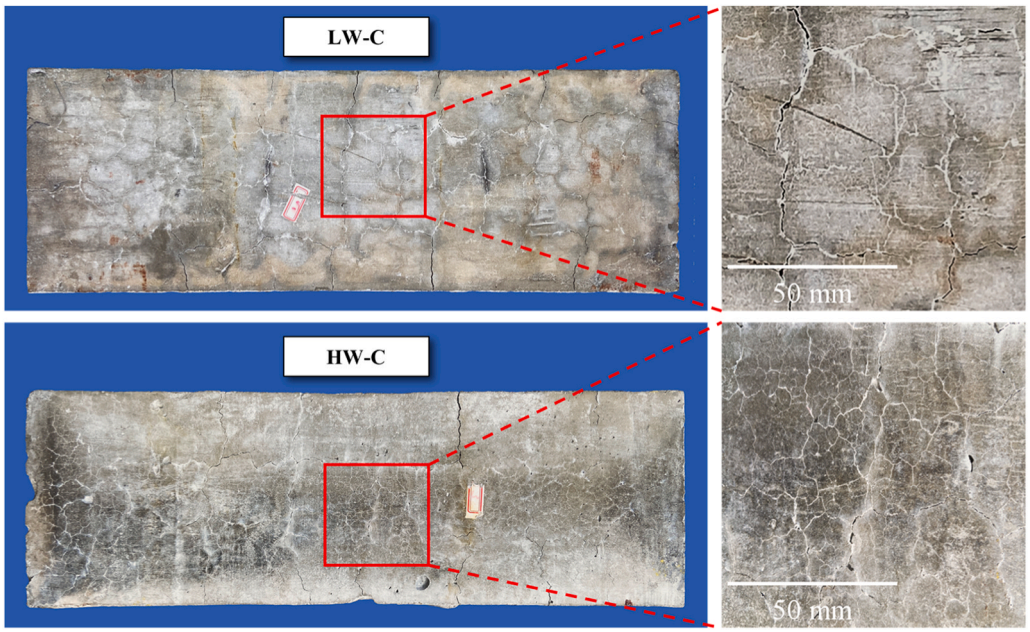

Fig. 10. Surface observations of columns after 30 days of water-CO_2 cyclic re-curing.

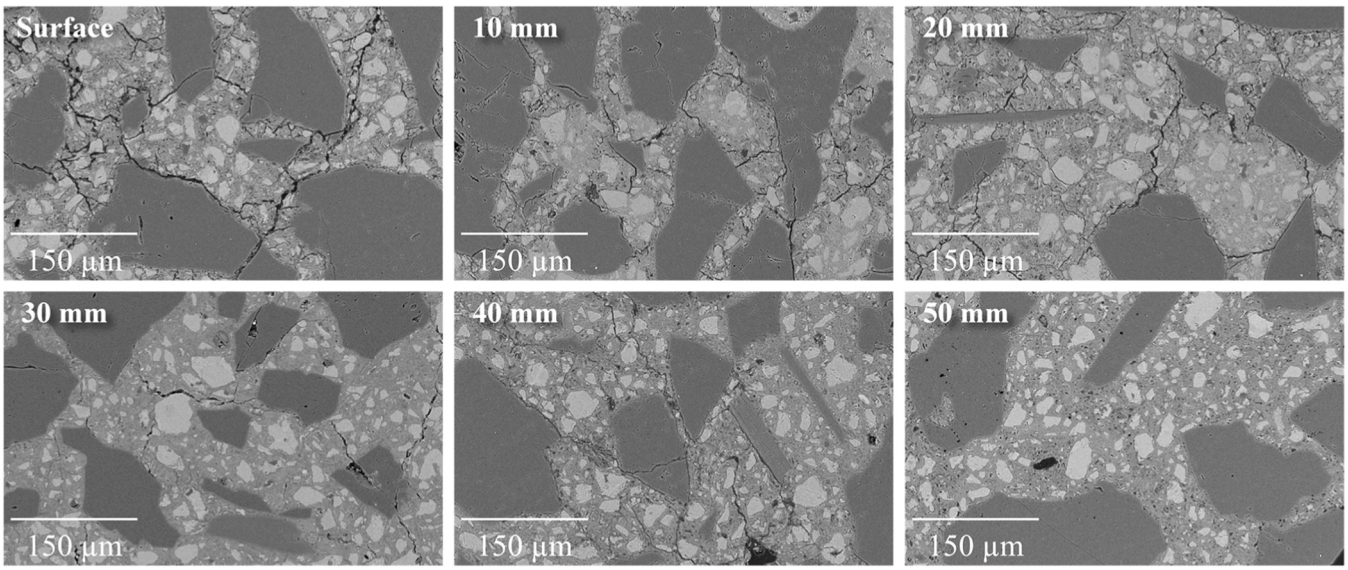

Fig. 11. BSE images of the LW-H column at different depths before re-curing.

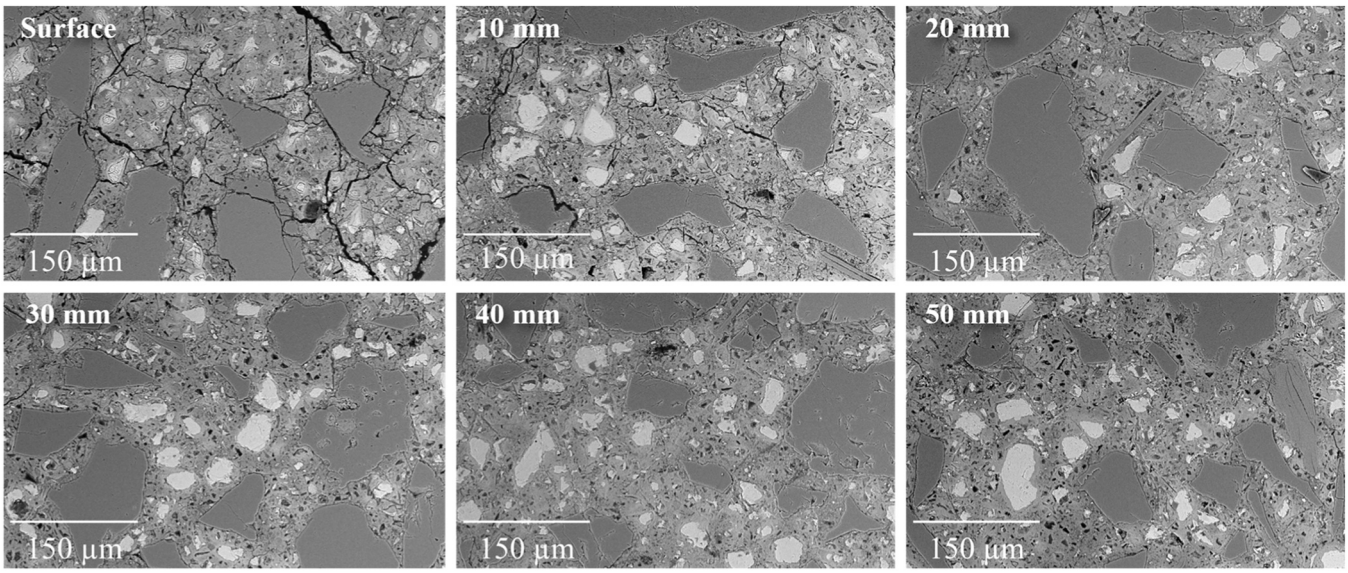

Fig. 12. BSE images of the HW-H column at different depths before re-curing.

through interpolation of thermocouple readings (Section 3.1). The calculated values are summarized in Table 5.

At elevated temperatures, concrete undergoes a series of decomposition reactions: ettringite (AFt) decomposes at 70–150 °C, calcium hydroxide (CH) decomposes at 400–500 °C, and calcium silicate hydrate (C-S-H) gel dehydrates gradually from 200 to 900 °C [47,70–72]. The dominant calcium silicate phase after exposure was β-C_2S, formed from the dehydration of C-S-H and the residual unhydrated cement [42,53].

At the surface (0–10 mm depth), both LW-H and HW-H columns exhibited severe microcracking within the interfacial transition zone (ITZ) and paste matrix. The cracks diminished in number and width with increasing depth. ITZ microcracks were primarily caused by thermal expansion mismatch between aggregates and paste, particularly due to the quartz α-β phase transition at 573 °C [26], which occurred only in the top 10 mm, matching the temperature distribution in Table 5. At 20 mm depth, ITZ cracking was nearly absent, while microcracks in the cement paste generally initiated above 400 °C [42,73]. From the temperature-depth data, the estimated depth at which such microcracking ceased was approximately 36 mm for the LW-H column and 19 mm for the HW-H column. At lower temperatures, microstructural

Table 5
Estimated peak temperatures at various depths within the columns.

Specimen ID	Maximum temperatures (°C)						
	10 mm	20 mm	30 mm	40 mm	50 mm	60 mm	100 mm
LW-H	649.6	451.6	419.4	387.2	355.0	322.8	305.5
HW-H	632.6	386.0	343.7	301.4	259.0	216.7	205.8

changes were dominated by pore coarsening caused by dehydration of C-S-H gel and decomposition of AFt.

Based on the temperature distribution and BSE observations, phase transformations and degradation patterns at different depths can be summarized as follows. In the LW-H column, Decomposition of AFt and dehydration of C-S-H occurred throughout the cross-section, causing widespread pore coarsening. CH decomposition and partial recrystallization of C-S-H [74,75] were evident up to 30 mm depth, leading to matrix cracking. Further C-S-H breakdown above 600 °C (≈10 mm depth) caused severe paste disintegration near the surface [76]. For the HW-H column, although AFt decomposition extended throughout the section, the dehydration of C-S-H was less pronounced across the cross section, where temperatures were lower than that of the LW-H column. CH decomposition and C-S-H recrystallization were mostly limited to the outermost 10 mm, creating a much shallower and more localized damage zone.

After 30 days of water-CO_2 cyclic re-curing, BSE images of the LW-C and HW-C columns (Fig. 13 and Fig. 14) revealed a marked densification of the cement matrix across all depths. The re-curing process promoted both rehydration and carbonation, leading to the partial healing of microcracks and the refinement of coarsened pores. To further clarify the phase evolution of unhydrated cement particles and the dehydrated matrix during the re-curing process, energy-dispersive X-ray spectrometry (EDS) analyses were conducted on samples extracted at a depth of 20 mm from both fire-damaged and re-cured columns. For each sample, eight measurement points were collected separately from regions corresponding to unhydrated cement particles and hydration products.

During the water-immersion phase, ionic diffusion was reactivated within the damaged matrix. Ca^{2+} and OH^- ions from unhydrated cement particles and high-temperature decomposition products (β-C_2S) dissolution migrated into the crack network formed by microcracks and voids left by melted PP fibers. Supersaturation of the pore solution induced the precipitation of rehydration products such as C-S-H gel, CH, and AFt [77].

During the subsequent carbonation phase, CO_2 diffused into the concrete and reacted with both newly formed and pre-existing hydration products. Calcium hydroxide (CH) underwent carbonation to form $CaCO_3$ and water, while unhydrated calcium silicates and β-C_2S reacted to produce silica gel and additional $CaCO_3$. The precipitation of calcite crystals within pores and microcracks induced a volumetric expansion of approximately 11–12 % [78,79], effectively sealing voids and densifying the matrix. At the outer surface (0–10 mm depth), this process was coupled with rehydration of residual unhydrated cement and β-C_2S formed during fire exposure, generating new C-S-H and CH phases that subsequently carbonated to yield dense $CaCO_3$ deposits. With increasing depth, unhydrated cement particles dominated the reactivity, leading to progressive pore filling and microcrack closure. After approximately five full water-CO_2 cycles, nearly all CH was converted to $CaCO_3$, and most cracks were sealed with tightly packed calcite. However, due to limited CO_2 diffusivity under the adopted conditions, the densification effect decreased beyond ~40 mm, where healing became less pronounced.

Fig. 15 presents the EDS results by plotting the atomic Si/Ca ratio against the atomic (Al + Fe)/Ca ratio. The data points corresponding to cement particle regions can be divided into two sub-clusters, representing C_4AF-rich phases and unhydrated calcium silicate phases, respectively. After 30 days of re-curing, a clear increase in the Si/Ca ratio was observed in the unhydrated calcium silicate region, indicating leaching of Ca^{2+} from these particles during the re-curing process. Concurrently, Ca^{2+} leaching from cement particles contributed to a decrease in the Si/Ca ratio within the hydration product regions. Since AFt preferentially precipitates within microcracks [42], variations in the (Al + Fe)/Ca ratio were observed in the hydration product regions. An increase in (Al + Fe)/Ca at certain points suggests pronounced AFt deposition, whereas a decrease in this ratio at other locations indicates leaching of $Al(OH)_4^-$ ions. In addition, a considerable number of points in the hydration product regions exhibited markedly reduced Si/Ca ratios, implying the formation of Ca-rich phases such as CH and $CaCO_3$. Combined with the abundant $CaCO_3$ crystals observed at the same depth in cross-sectional samples (yellow boxed regions in Fig. 13 and Fig. 14), these results indicate that carbonation penetrated to a depth of 20 mm, further densifying the HPC matrix.

The microstructural evolution clearly reflected the gradient of both damage and recovery. To contextualize these results, Fig. 16 compares representative BSE micrographs from previous studies [41,42] with those from the present investigation. The compressive-strength recovery ratios reported in those references are annotated in the lower-right corners of each image.

For the LW system, the 10 mm-depth microstructure of the LW-H column closely resembled that of reference specimen REF-0.18–600-H, while the surface layer corresponded to REF-0.18–800-H, consistent with the internal temperature distribution. Although microcracking extended to approximately 40 mm, severe degradation was confined to the outer 30 mm, and below 50 mm the matrix remained largely unaffected. After re-curing, the LW-C column exhibited microstructural

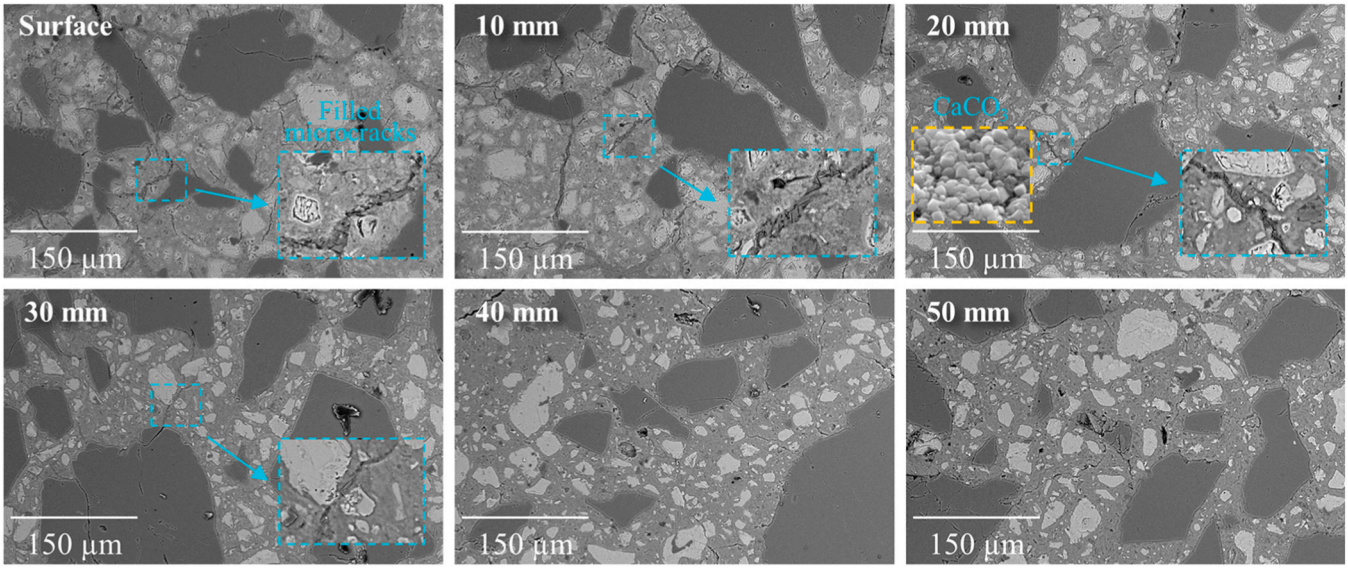

Fig. 13. BSE images of concrete in the LW-C column after re-curing.

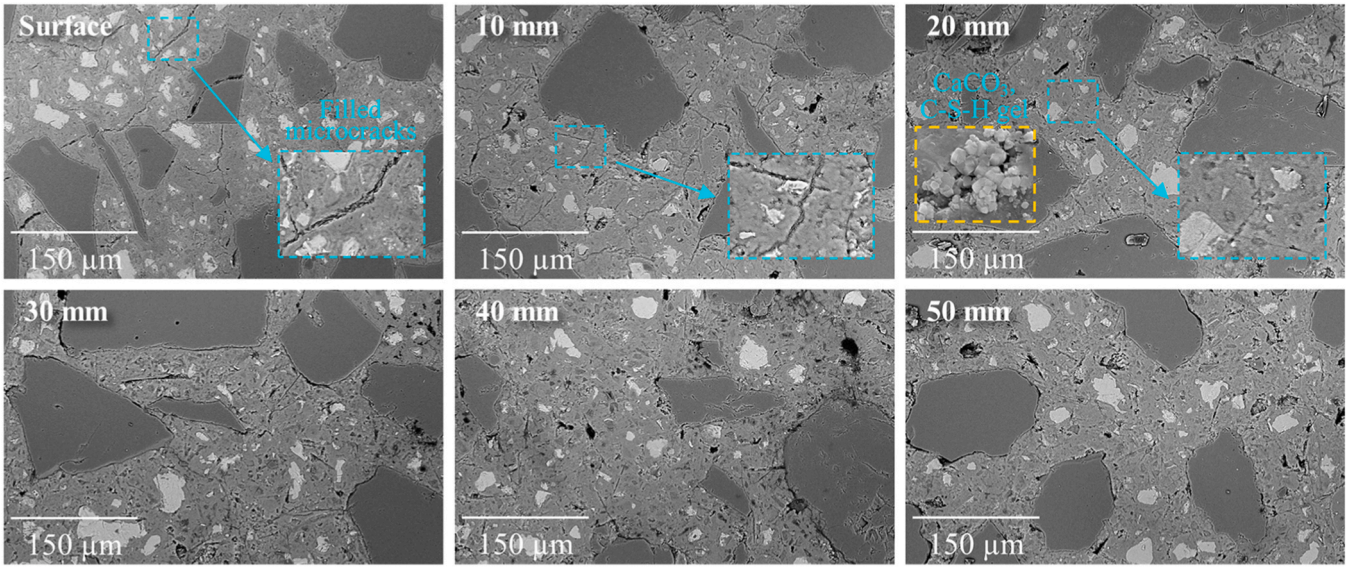

Fig. 14. BSE images of concrete in the HW-C column after re-curing.

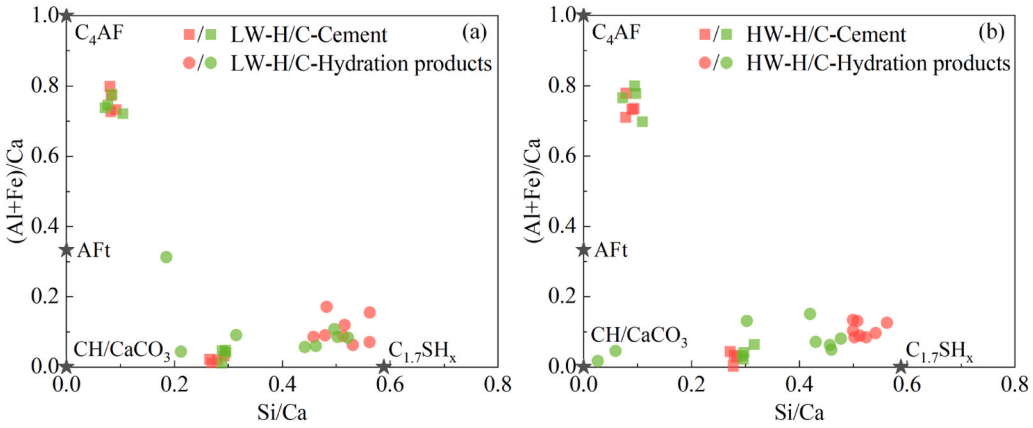

Fig. 15. The molar (Al + Fe)/Ca as a function of the molar Si/Ca of the HPC columns after fire exposure and re-curing at the depth of 20 mm: (a) LW columns; (b) HW columns.

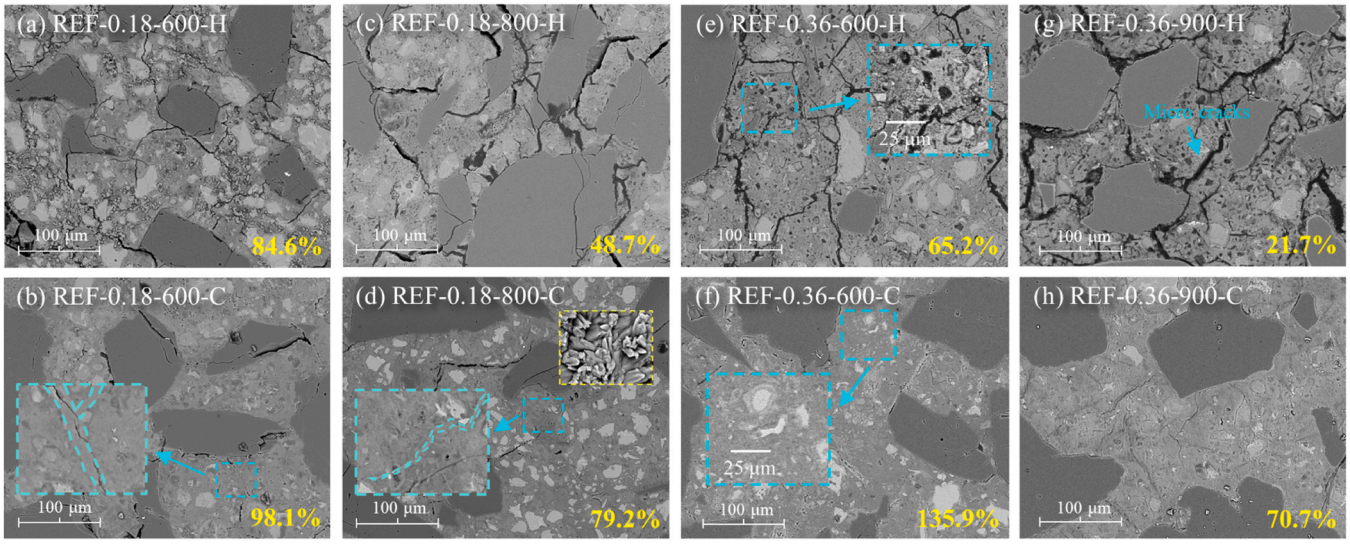

Fig. 16. BSE images from references [41,42], illustrating microstructural change after heat exposure (H) and re-curing (C).

features comparable to REF-0.18–600-C and REF-0.18–800-C, which in earlier work regained 98.1 % and 79.2 % of their original compressive strengths, respectively [42]. This suggests that the strength deficit in the present LW-C column was confined mainly to the top 10 mm surface layer.

For the HW system, the surface microstructure of the HW-H column was intermediate between REF-0.36–600-H and REF-0.36–900-H, as its surface temperature did not exceed 900 °C. Although microcracks were still visible at 10 mm depth, their density and width were smaller than those reported in REF-0.36–600-H. Significant strength degradation was limited to the upper 10 mm, while microcrack initiation corresponded to the 400 °C isotherm (10–20 mm depth). Following re-curing, the HW-C column's microstructure became fully densified, particularly in the 10–20 mm region, where local strength likely surpassed its original value.

Overall, the water-CO_2 cyclic re-curing process effectively reversed the key microstructural deterioration mechanisms of fire-damaged HPC. Rehydration and carbonation collectively sealed microcracks, re-filled coarsened pores, and reinstated the stiffness of the cement matrix. The recovery depth and extent depended on the thermal damage gradient: while the LW-C column achieved partial restoration (limited by deeper macrocracking), the HW-C column exhibited nearly complete microstructural recovery, consistent with its mechanical strength restoration discussed in Section 4 [41,53,80].

3.4. Load-bearing capacity test results

3.4.1. Failure patterns

The failure patterns of all columns are illustrated in Figs. 17–19. Columns tested at ambient temperature exhibited stable mechanical performance throughout most of the loading process. As shown in Fig. 17, both LW-A and HW-A columns maintained structural integrity without visible cracking or deformation until approximately 90 % of their peak load. Near the ultimate stage, audible cracking indicated the initiation of internal damage. With further loading, longitudinal cracks developed progressively, and the concrete core began to expand. At peak load, the LW-A column experienced localized edge spalling and crushing of the cover, resulting in a sharp post-peak load drop. The failure mode was characterized by localized cover spalling and surface cracking, typical of ductile compression failure with moderate post-peak deformability.

After fire exposure, both columns exhibited pronounced changes in failure pattern (Fig. 18). Compared with their pre-test condition (Fig. 10), transverse cracks on the fire-damaged columns became less visible after failure, whereas longitudinal cracks widened substantially. This transformation reflected the reduced elastic modulus of HPC following thermal exposure [11,81,82], which caused greater axial deformation under load. The combined effects of pre-existing temperature-induced cracking and reduced stiffness promoted lateral expansion of the core concrete during compression [83,84].

In the LW-H column, the protective layer at mid-height spalled and fractured after peak loading, whereas the remaining regions showed minor surface damage. This behavior suggests that the overall failure mechanism remained similar to that of the unheated column - cover spalling accompanied by localized core crushing. In contrast, the HW-H column displayed more extensive surface spalling and distinct diagonal shear cracks. This more severe failure pattern is attributed to the greater degradation of mechanical properties in the HW mix, particularly within the surface region exposed to 400–800 °C [41,42]. Although both columns ultimately failed in a ductile compression mode, the HW-H specimen exhibited more extensive cracking and weaker confinement of the core concrete.

Following 30 days of water-CO_2 cyclic re-curing, the C-series columns displayed improved surface integrity, though their overall failure mechanisms remained consistent with those of the fire-damaged specimens (Fig. 19). Longitudinal cracks formed during fire exposure reopened under loading, indicating that the recovery of tensile capacity across these cracks was limited. Nevertheless, noticeable improvements were observed in crack distribution and surface cohesion. In the LW-C column, protective-layer spalling shifted from mid-height to the corners, suggesting a redistribution of internal stress and partial strengthening of the outer zone. The HW-C column exhibited reduced spalling extent and fewer diagonal cracks, confirming that re-curing enhanced the mechanical resistance and bonding continuity of the cover concrete.

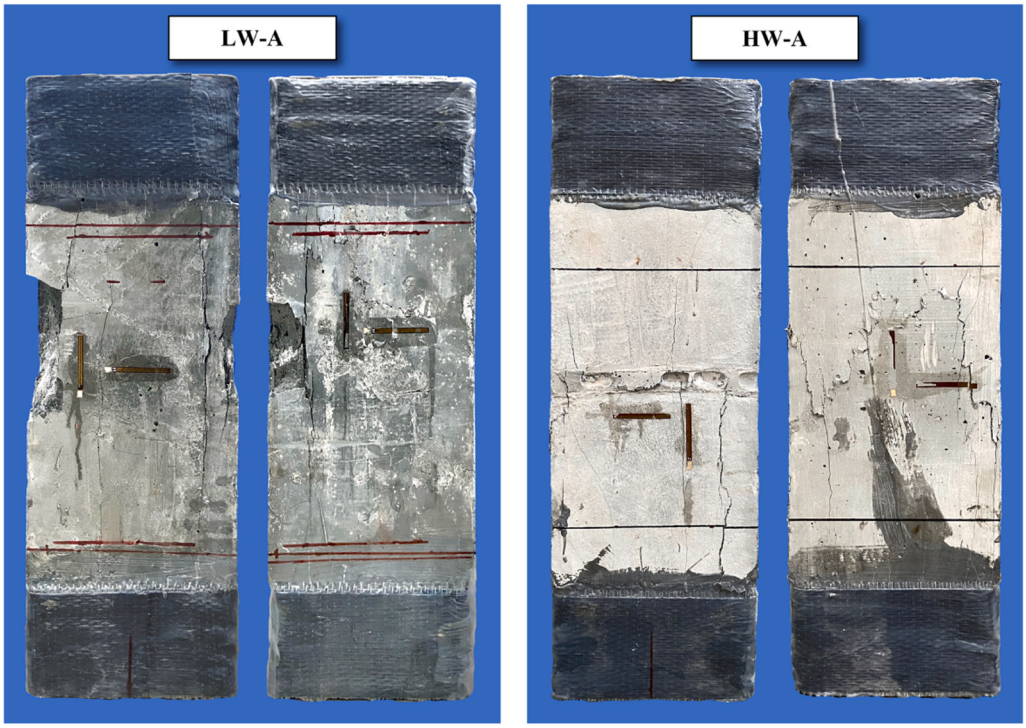

Fig. 17. Failure patterns of columns at ambient temperature.

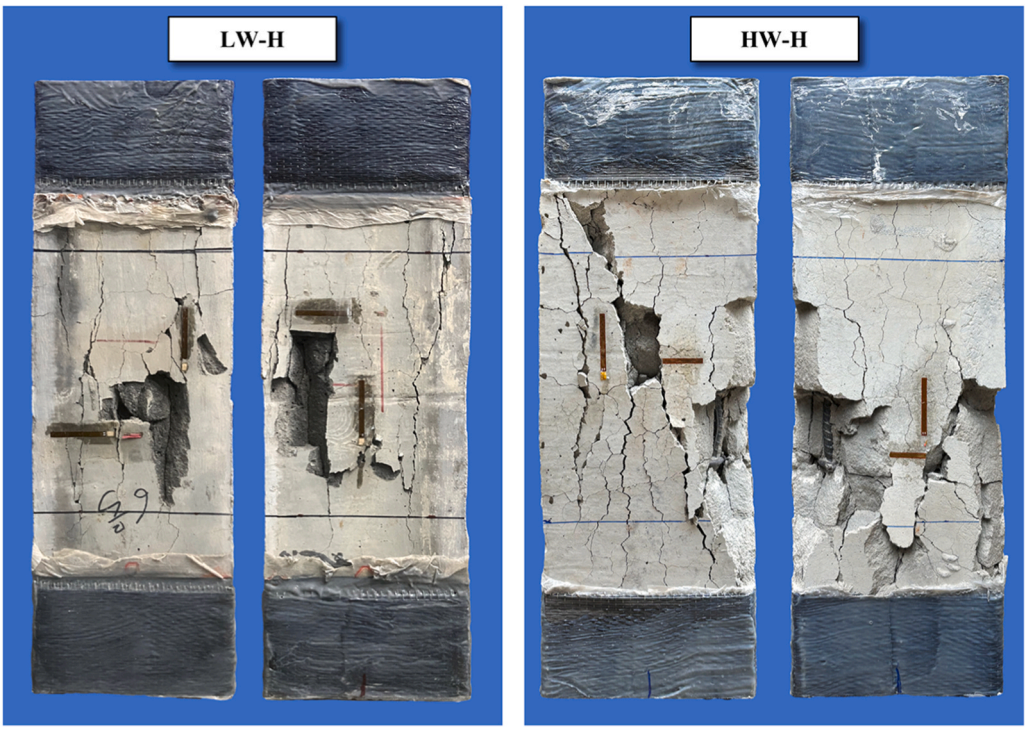

Fig. 18. Failure patterns of columns after fire exposure.

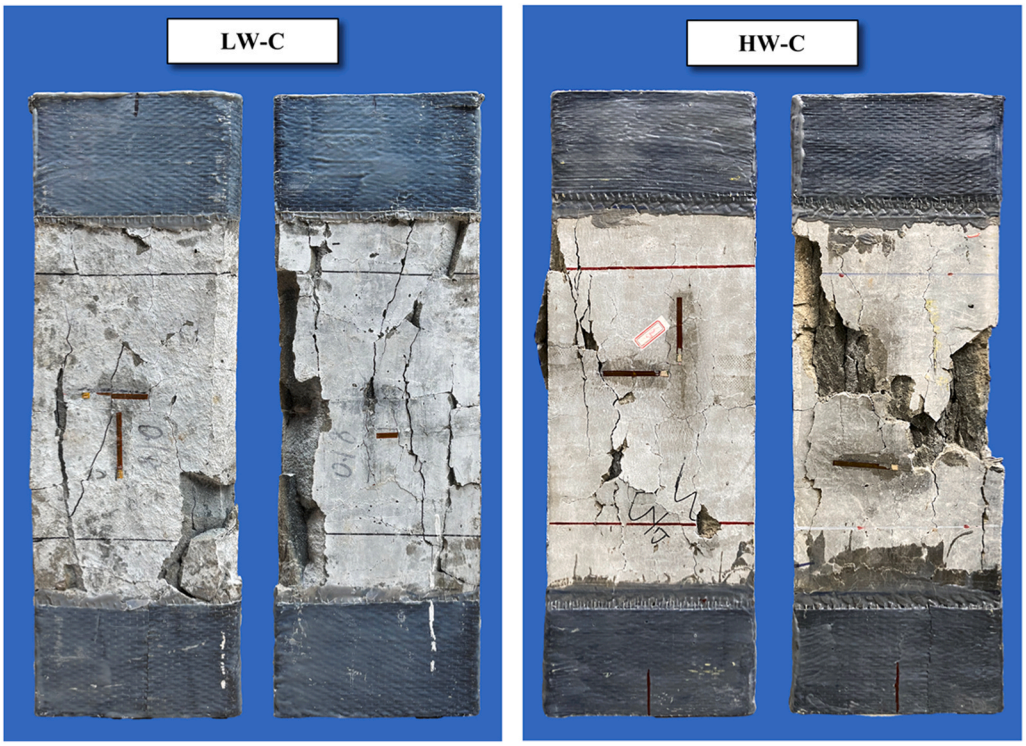

Fig. 19. Failure patterns of columns after re-curing.

Comparative analysis of all three series, A (ambient), H (fire-damaged), and C (re-cured), reveals clear trends. For the HW mixture, fire exposure significantly weakened the outer concrete, promoting cover spalling along pre-existing longitudinal cracks. Water-CO_2 re-curing improved surface strength and delayed spalling onset, indicating partial recovery [85,86]. For the LW mixture, fire-induced expansion and internal cracking of the dense core dominated the failure process. Re-curing increased the elastic modulus and reduced deformation but could not completely eliminate longitudinal cracking. These observations confirm that while cyclic re-curing substantially restores compressive strength and cohesion, full recovery of tensile integrity and core confinement remains limited in severely

heat-damaged, low-W/B HPC columns.

3.4.2. Load-bearing capacity and stiffness

The ultimate load-bearing capacity and stiffness of all columns are summarized in Fig. 20. For the ambient-temperature columns, stiffness was determined from the load-displacement ratio at 40 % of the peak load. For the fire-damaged and re-cured columns, the initial segment of the load-displacement curve exhibited slight instability due to residual thermal expansion [87] and crack closure effects (see Fig. 21). Therefore, post-fire and post-recuring stiffness values were evaluated from the stabilized linear region between 25 % and 40 % of the peak load.

Fire exposure caused substantial reductions in both ultimate capacity and stiffness for all specimens. The LW-A column initially carried an ultimate load of 4088.8 kN with a stiffness of 8232.9 kN/mm. After fire exposure, the LW-H column's capacity and stiffness decreased to 2040.0 kN and 1582.8 kN/mm, representing reductions of 50.1 % and 80.8 %, respectively. The HW-A column originally exhibited a capacity of 2036.1 kN and a stiffness of 3246.3 kN/mm, which decreased to 1630.2 kN and 930.5 kN/mm in the HW-H column, reductions of 19.9 % and 71.3 %, respectively.

Although both concretes suffered pronounced stiffness degradation, the LW-H column experienced a much greater loss of load-bearing capacity. This difference reflects the higher internal temperatures and deeper damage in the denser, low-W/B mixture, as discussed in Sections 3.1 and 3.3. Elevated temperatures induced microcrack propagation, pore coarsening, and decomposition of hydration products, collectively reducing both compressive strength and elastic modulus. Since the elastic modulus is more sensitive to microstructural deterioration than compressive strength [11,81,82], this explains the disproportionately large stiffness reduction observed.

Water-CO_2 cyclic re-curing produced significant mechanical recovery. In the LW-C column, the ultimate load increased to 2753.6 kN and stiffness to 4850.5 kN/mm—35.0 % and 206.5 % higher than those of the fire-damaged state, corresponding to 67.3 % and 58.9 % of the original (unheated) values, respectively. The HW-C column achieved an ultimate load of 2054.1 kN and stiffness of 2006.9 kN/mm, marking increases of 26.0 % and 115.7 % relative to the fire-damaged condition. Remarkably, this represented a full recovery of the original load-bearing capacity (100.9 %) and a substantial restoration of stiffness (61.8 %). These findings demonstrate that the water-CO_2 cyclic re-curing process effectively promotes structural recovery of fire-damaged HPC columns by enhancing both material strength and stiffness. The LW mixture, despite its initially higher strength, exhibited deeper and more severe damage due to steeper thermal gradients, resulting in limited recovery. Conversely, the HW mixture, with shallower damage and higher residual reactivity, responded more effectively to re-curing, achieving near-complete mechanical restoration.

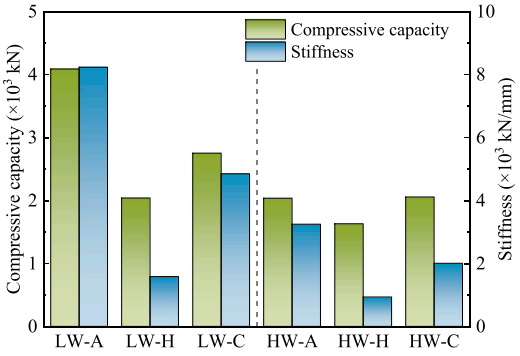

Fig. 20. Ultimate load-bearing capacity and stiffness of columns under ambient, fire-exposed, and re-cured conditions.

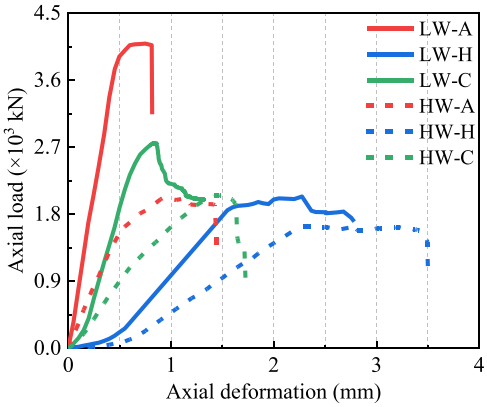

Fig. 21. Axial load-displacement curves of columns under ambient, fire-exposed, and re-cured conditions.

3.4.3. Load-displacement and strain response

Fig. 21 presents the axial load-displacement curves of the LW and HW columns under ambient, fire-damaged, and re-cured conditions. Ductility was assessed from these curves using the displacement-ductility index (μ), defined as the ratio between the axial displacement at 85 % of the peak load on the descending branch (Δ_{85}) and the displacement at peak load (Δ_y) [88,89]. The results are summarized in Table 6. The corresponding axial load-strain responses are shown in Fig. 22, where compressive strains are plotted as negative and tensile strains as positive. Because of signal noise and large local deformations beyond the peak load, only data up to the maximum load are reported.

Under ambient conditions, both LW-A and HW-A columns exhibited a well-defined linear-elastic stage in their load-displacement curves. When the displacement reached 0.5 mm, the strain in the longitudinal reinforcement reached 2000 με, initiating yielding and causing a slight reduction in stiffness. As the load approached the ultimate value, a yield plateau developed, reflecting the confinement provided by the stirrups against lateral expansion of the concrete core [90]. In the load-strain curves, both unheated columns showed linear behavior at early stages, followed by gradual stiffness reduction as they neared peak load. Post-peak softening occurred through localized crushing and surface spalling. The HW-A column demonstrated slightly higher ductility than the LW-A column, attributable to its lower matrix brittleness [91,92] and the more effective stirrup confinement afforded by its weaker concrete [90].

For the fire-damaged (H-series) columns, residual thermal expansion and the closure of pre-existing transverse cracks governed the initial portion of the load-displacement curve. At the beginning of loading, the curves displayed an initially shallow slope that gradually increased as cracks closed and internal stress equilibrium was re-established. Once these cracks were compressed, the response became linear until approaching the peak load. Strain gauges were positioned to avoid major visible cracks. Consequently, the load-strain curves (Fig. 22) did not exhibit the initial stiffening seen in the displacement curves, confirming that the low-stiffness region corresponded to the crack-closure stage rather than material softening.

Due to the difficulty of avoiding diagonal narrow cracks when

Table 6
Ductility performance of columns.

Specimen ID	Δ_y (mm)	Δ_{85} (mm)	μ
LW-A	0.75	0.82	1.09
LW-H	2.28	2.75	1.21
LW-C	0.83	0.94	1.13
HW-A	0.95	1.44	1.52
HW-H	2.25	3.50	1.56
HW-C	1.51	1.64	1.09

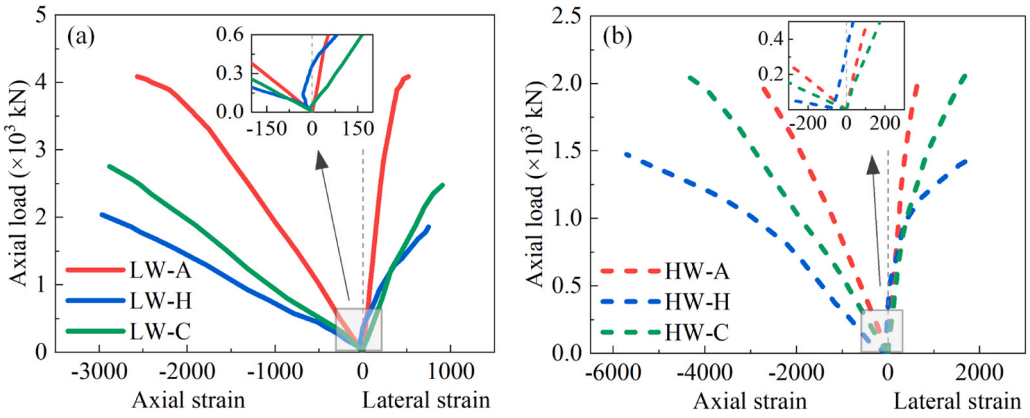

Fig. 22. Axial load-strain curves of columns under ambient, fire-exposed, and re-cured conditions.

attaching lateral strain gauges, the load–lateral strain responses showed that lateral strain was initially compressive and then became tensile as the cracks intersected by the gauges were compressed and reopened. After thermal exposure, stiffness loss and longitudinal cracking weakened confinement [93]. In HW-H, the cover retained partial integrity at lower loads, so confinement remained effective; however, crack interconnection in the cover caused a rapid drop in confinement effectiveness and a sharp acceleration of lateral strain rate at higher loads. In contrast, LW-H had deeper, more continuous longitudinal macrocracks from the early loading stage, leading to a more progressive increase in lateral deformation without a distinct transition. Earlier stirrup yielding produced an extended plateau, while the reduced compressive strength enhanced the relative contribution of stirrup confinement.

Following 30 days of water-CO_2 cyclic re-curing, the load-displacement curves of both LW-C and HW-C columns exhibited a steeper initial slope and a shorter low-stiffness segment, indicating that the rehydration and carbonation products largely eliminated crack closure stage. The absence of compressive strain readings at the beginning of loading confirmed that rehydration and carbonation products had filled most surface cracks, allowing the matrix to participate in load transfer from the onset of loading.

The post-peak response of the re-cured columns became noticeably sharper, indicating that re-curing enhanced compressive strength and stiffness but also structural brittleness [94,95]. For the LW-C column, ductility decreased modestly (6.6 %) compared to the fire-damaged state, whereas the HW-C column exhibited a more significant reduction (30.1 %). This difference is attributed to the greater stiffness and strength recovery in the HW-C specimen, which reduced the relative effectiveness of stirrup confinement and limited the development of plastic deformation. In addition, the re-curing products formed through rehydration and carbonation improve compressive resistance and matrix continuity, while providing limited enhancement in tensile strength across pre-existing macrocracks. As a result, tensile continuity and energy dissipation capacity are not fully restored, leading to a stiffer yet more brittle post-peak response. Strength recovery therefore does not necessarily imply restoration of deformation capacity.

Both re-cured columns still displayed lower stiffness than their unheated counterparts, indicating that the elastic modulus was only partially restored. As shown in Fig. 22, lateral expansion of the re-cured columns remained greater than that of the A-series columns, reflecting incomplete recovery of tensile integrity provided by re-curing products with in the pre-existing longitudinal cracks. These residual weaknesses limited the ability of the core concrete to fully restrain dilation, thereby constraining further gains in overall load-bearing capacity.

3.4.4. Calculation of load-bearing capacity

To evaluate the residual axial load-bearing capacity of the fire-damaged and re-cured columns, analytical predictions were compared with experimental results using the isotherm method, as recommended by Eurocode 2 [54]. This approach assumes that all material within a specified isothermal depth has lost its mechanical properties due to thermal degradation. The unaffected inner core is treated as the effective load-bearing section.

The total axial capacity N_R of a column subjected to high temperature can be expressed as [54]:

$$N_R = A_c f_{ck,20} + A_s \varphi_y f_{sy,20} \quad (2)$$

where $f_{ck,20}$ is the original strength of concrete, $f_{sy,20}$ is the original strength of steel reinforcement with a temperature-dependent reduction coefficients φ_y applied [96]. A_c and A_s are the areas of concrete core and reinforcement that remain effective after exposure.

The temperature distribution across the section was interpolated from measured thermocouple data (Section 3.1) and converted to a temperature-depth curve (Fig. 8). Based on EN 1992–1–2:2004 [54], concrete layers exceeding 500 °C are considered structurally ineffective. For LW-H with a higher strength and extended internal cracking, this threshold is often reduced to between 500 °C and 400 °C, reflecting its increased sensitivity to thermal degradation [5,54,97].

As shown in Table 7, the 500 °C isotherm criterion provided a satisfactory prediction for the HW-H column, with only a 3.0 % deviation from the experimental value. However, for the LW-H column, this approach significantly overestimated the actual load-bearing capacity, mainly because of the deeper penetration of heat and the greater internal damage caused by its dense matrix. When the limiting temperature was reduced to 400 °C, the predicted value (1895.0 kN) aligned closely with the experimental result (2040.0 kN).

4. Discussion

This study systematically investigated the temperature history, failure patterns, microstructural evolution, and mechanical responses of reinforced HPC columns after fire exposure, with the aim of clarifying the mechanisms governing load-bearing capacity degradation and subsequent recovery at the structural scale. The results demonstrate that post-fire structural degradation arises from the coupled effects of material deterioration and macro-scale cracking, rather than from compressive strength loss alone.

Under post-fire axial loading, the reduction in compressive strength and elastic modulus [11,98], together with unclosed macrocracks and residual thermal deformation [84], resulted in increased axial and lateral deformation, thereby accelerating the failure process. Two mechanisms were identified to govern post-fire capacity degradation: (i) material-level deterioration caused by dehydration, decomposition, and phase transformation of hydration products accompanied by high-temperature-induced microcracking [41], and (ii) amplification of

Table 7
Comparison between analytical and experimental load-bearing capacities.

Column	A_c (mm^2)	$f_{ck,\ 20}$ (MPa)	φ_y	A_s (mm^2)	$f_{sy,\ 20}$ (MPa)	N_R (kN)	P_{test} (kN)	N_R / P_{test}
LW-H (use 500 °C isotherm)	26736.2	104.4	0.95	452.4	432.0	2835.2	2040.0	1.39
LW-H (use 400 °C isotherm)	16373.3					1895.0	2040.0	0.93
HW-H (use 500 °C isotherm)	28191.3	53.1				1682.6	1630.2	1.03

Note: P_{test} is the residual compressive capacity test value of the columns.

lateral strain due to stiffness loss and thermally induced macrocrack propagation, which weakened the confinement effectiveness of the core concrete.

Microstructural observations confirmed that temperature-dependent damage of the cementitious matrix is the primary driver of material strength degradation. The depth-dependent variation in microcrack density and pore coarsening showed a close correspondence with the measured temperature profiles. Compared with the HW-H column, the LW-H column experienced higher internal temperatures and more pronounced thermal gradients, leading to deeper and more extensive microcracking.

Differences in temperature histories between the LW-H and HW-H columns further influenced the structural response through their effects on cracking. Larger internal temperature gradients in the LW-H column generated higher thermal stresses and promoted deeper propagation of macrocracks. During cooling, tensile stresses developed near the concrete surface, contributing to additional crack formation. Upon axial compression, these pre-existing cracks accelerated lateral dilation of the core concrete, resulting in failure modes dominated by cover spalling and core expansion. Consequently, columns exposed to higher peak temperatures and larger temperature gradients exhibited more severe structural degradation and greater reductions in load-bearing capacity.

Although HPC generally retains a relatively high proportion of its intrinsic compressive strength after exposure to temperatures of 400–600 °C, the present results indicate that macro-scale cracking and stiffness degradation play a dominant role in governing post-fire structural performance. These effects, driven by non-uniform temperature exposure [99], significantly reduce global load-bearing behavior and should therefore be explicitly incorporated into structural-level post-fire assessment and predictive models.

The mechanisms responsible for strength recovery were elucidated through combined microstructural observations and structural testing of the re-cured columns. The water-CO_2 cyclic re-curing process effectively mitigated the two dominant degradation mechanisms by promoting alternating rehydration and carbonation reactions. These reactions filled microcracks and coarsened pores with hydration and carbonation products, leading to matrix densification and partial restoration of elastic modulus and compressive strength. The recovery of material strength contributed directly to the restoration of load-bearing capacity, while stiffness recovery moderated axial deformation and reduced lateral strain development under loading. In the present study, carbonation was inferred from microstructure observations, EDS analyses, and established findings in the literature [41,42,52], while direct measurement of carbonation depth across the column section was not conducted.

Nevertheless, the ability of re-curing to repair large macrocracks remained limited, particularly in regions subjected to severe thermal damage. As a consequence, tensile continuity in these zones was not fully restored, and localized strain concentration persisted during axial compression. The HW-C column, characterized by a well-recovered core and a moderately damaged cover, achieved full restoration of load-bearing capacity, whereas the LW-C column, which exhibited deeper macrocracking due to more severe internal thermal gradients, showed only partial recovery. It should also be noted that carbonation involved in the re-curing process may reduce concrete alkalinity and potentially increase the risk of reinforcement depassivation and corrosion if carbonation penetrates to the steel depth. In the proposed cyclic re-curing regime, lime-saturated water was deliberately adopted during the immersion stage to provide a highly alkaline environment, which may partially replenish or buffer the alkalinity of the near-surface pore solution prior to the carbonation stage. The influence of cyclic re-curing on alkalinity evolution, transportation properties, and reinforcement corrosion performance requires dedicated investigation in future work.

Finally, it should be noted that the column specimens adopted in this study (200 mm × 200 mm × 600 mm) are scaled relative to columns used in engineering practice. For columns with larger cross-sections, the penetration depth of temperature-gradient-induced macrocracking and thermal decomposition-induced microcracking are expected to be comparable, as they are governed by local temperature history and temperature-controlled reactions rather than by global member size [5,100]. Consequently, the depth-dependent damage patterns identified in this study and the associated re-curing mechanisms remain applicable in principle to larger members. Nevertheless, as the cross-sectional dimensions increase, the fire-damaged zone constitutes a smaller fraction of the load-bearing section, leading to higher residual capacity and a reduced apparent contribution of re-curing to global strength recovery. The results presented herein should therefore be interpreted as mechanistic rather than directly quantitative for full-scale columns. Future work should couple the present findings with section-level thermal analysis and simplified damage-zoning models to enable rational post-fire assessment and repair design for full-scale reinforced concrete columns.

5. Conclusions

This study investigated the fire-induced degradation and post-fire recovery of reinforced high-performance concrete (HPC) columns through a comprehensive experimental program that included thermal exposure, mechanical testing, and microstructural characterization. The principal conclusions are as follows:

1. The low water-to-binder (LW) mixture developed steeper internal temperature gradients and higher internal temperatures than the high water-to-binder (HW) mixture, leading to deeper penetration of macro-scale cracks and more extensive strength degradation after fire exposure.
2. Post-fire failure was governed by lateral expansion and cover spalling, accelerated by longitudinal macrocracks and severe stiffness loss. As a result, the LW-H column experienced significantly greater capacity loss (50.1 %) than the HW-H column (19.9 %), demonstrating the higher vulnerability of HPC with a low water-to-binder ratio and low porosity to thermal-gradient-induced damage.
3. The Eurocode-based 500 °C isotherm method provided accurate capacity prediction for the HW-H column but overestimated the capacity of the LW-H column. A reduced limiting temperature of 400 °C yielded better agreement, indicating that low-porosity, low-permeability HPC requires more conservative damage thresholds.
4. Water-CO_2 cyclic re-curing effectively restored mechanical performance by promoting rehydration and carbonation, which sealed microcracks and densified the matrix. Full strength recovery was

achieved in the HW-C column (100.9 %), whereas recovery in the LW-C column was limited (67.3 %) by deeper macrocracking, highlighting that restoration of large cracks and tensile continuity remains a key challenge.

CRediT authorship contribution statement

Ye Li: Writing – review & editing, Validation, Resources, Project administration, Methodology, Investigation, Funding acquisition, Conceptualization. **Tiejun Liu:** Resources, Project administration, Investigation, Funding acquisition. **Dujian Zou:** Validation, Supervision, Methodology, Formal analysis. **Hangqi Lou:** Writing – original draft, Visualization, Validation, Investigation, Formal analysis, Data curation.

Declaration of Competing Interest

The authors declare that they have no known competing financial interests or personal relationships that could have appeared to influence the work reported in this paper.

Acknowledgments

This work was supported by the National Science Fund for Distinguished Young Scholars (No. 52025081), the National Natural Science Foundation of China (No. 52378229), Guangdong Provincial Key Laboratory of Intelligent and Resilient Structures for Civil Engineering (2023B1212010004).

Data Availability

Data will be made available on request.

References

[1] DenariÉ E, BrÜhwiler E. Structural rehabilitations with ultra-high performance fibre reinforced concretes (UHPFRC). Restor Build Monum 2006;12:93–108.
[2] A.K. Tovey, Assessment and repair of fire-damaged concrete structures-an update. ACI Symposium Publication, 92 47-62.
[3] Ma WX, Yin CX, Zhou J, Wang L. Repair of fire-damaged reinforced concrete flexural members: a review. Sustainability 2019;11.
[4] Zhou J, Wang L. Repair of fire-damaged reinforced concrete members with axial load: a review. Sustainability 2019;11.
[5] Kodur VKR, Raut NK, Mao XY, Khaliq W. Simplified approach for evaluating residual strength of fire-exposed reinforced concrete columns. Mater Struct 2013;46:2059–75.
[6] Kodur V, Alogla SM, Venkatachari S. Guidance for treatment of high-temperature creep in fire resistance analysis of concrete structures. Fire Technol 2021;57:1167–97.
[7] Malik M, Bhattacharyya SK, Barai SV. Thermal and mechanical properties of concrete and its constituents at elevated temperatures : a review. Constr Build Mater 2021;270:121398.
[8] Li Y, Tan KH, Yang EH. Influence of aggregate size and inclusion of polypropylene and steel fibers on the hot permeability of ultra-high performance concrete (UHPC) at elevated temperature. Constr Build Mater 2018;169:629–37.
[9] Choe G, Kim G, Kim H, Hwang E, Lee S, Son M, et al. Influence of amorphous metallic fibers on spalling properties of high-strength concrete exposed to high temperature. Constr Build Mater 2020;263:120711.
[10] Li Y. Effect of post-fire curing and silica fume on permeability of ultra-high performance concrete. Constr Build Mater 2021;290.
[11] Chen YH, Chang YF, Yao GC, Sheu MS. Experimental research on post-fire behaviour of reinforced concrete columns. Fire Saf J 2009;44:741–8.
[12] Kodur VKR. Spalling in high strength concrete exposed to fire: concerns, causes, critical parameters and cures. Adv Technol Struct Eng 2012:1–9.
[13] Kodur VKR, Wang TC, Cheng FP. Predicting the fire resistance behaviour of high strength concrete columns. Cem Concr Compos 2004;26:141–53.
[14] Behnood A, Ziari H. Effects of silica fume addition and water to cement ratio on the properties of high-strength concrete after exposure to high temperatures. Cem Concr Compos 2008;30:106–12.
[15] Li Y, Yang EH, Tan KH. Effects of heating followed by water quenching on strength and microstructure of ultra-high performance concrete. Constr Build Mater 2019;207:403–11.
[16] Fares H, Remond S, Noumowe A, Cousture A. High temperature behaviour of self-consolidating concrete: microstructure and physicochemical properties. Cem Concr Res 2010;40:488–96.
[17] Yazıcı H, Deniz E, Baradan B. The effect of autoclave pressure, temperature and duration time on mechanical properties of reactive powder concrete. Constr Build Mater 2013;42:53–63.
[18] Ramzi S, Moradi MJ, Hajiloo H. The study of the effects of supplementary cementitious materials (SCMs) on concrete compressive strength at high temperatures using artificial neural network model. Buildings 2023;13.
[19] Shahraki M, Hua N, Elhami-Khorasani N, Tessari A, Garlock M. Residual compressive strength of concrete after exposure to high temperatures: a review and probabilistic models. Fire Saf J 2023;135.
[20] Li Y, Pimienta P, Pinoteau N, Tan KH. Effect of aggregate size and inclusion of polypropylene and steel fibers on explosive spalling and pore pressure in ultra-high-performance concrete (UHPC) at elevated temperature. Cem Concr Compos 2019;99:62–71.
[21] Pan Z, Sanjayan JG, Kong DLY. Effect of aggregate size on spalling of geopolymer and Portland cement concretes subjected to elevated temperatures. Constr Build Mater 2012;36:365–72.
[22] Liu Y, Tan KH, Du Y, Su J, Hu X, Mao Y, et al. Comparison of axial behavior of RC columns using alkali-activated slag-based concrete and OPC concrete during and after fire. J Build Eng 2023;77:107444.
[23] Kadhum MM, Hashim AM, Khamees SS, Akhaveissy AH, Ali AH. Experimental investigation of fire effects under axial compression on ductility and stiffness of (SIFCON) columns. Struct Concr 2022;23:3554–68.
[24] Zhao J, Zheng J-j, Peng G-f, van Breugel K. A meso-level investigation into the explosive spalling mechanism of high-performance concrete under fire exposure. Cem Concr Res 2014;65:64–75.
[25] Fu YF, Wong YL, Tang CA, Poon CS. Thermal induced stress and associated cracking in cement-based composite at elevated temperatures - Part I: thermal cracking around single inclusion. Cem Concr Compos 2004;26:99–111.
[26] Fu YF, Wong YL, Poon CS, Tang CA. Numerical tests of thermal cracking induced by temperature gradient in cement-based composites under thermal loads. Cem Concr Compos 2007;29:103–16.
[27] Akca AH, Özyurt N. Effects of re-curing on residual mechanical properties of concrete after high temperature exposure. Constr Build Mater 2018;159:540–52.
[28] Li LS, Wang Y, An MZ, Yu PY, Hou X. The Influence of rehydration on the oroperties of portland cement-based materials with low water/binder ratios: a review of existing research. Materials 2023;16:970.
[29] He FZ, Biolzi L, Carvelli V. Effects of elevated temperature and water re-curing on the compression behavior of hybrid fiber reinforced concrete. J Build Eng 2023;67:106034.
[30] Bouhafs F, Ezziane M, Ayed K, Leklou N, Mouli M. Effect of water re-curing on the physico-mechanical and microstructural properties of self-compacting concrete reinforced with steel fibers after exposure to high temperatures. Constr Build Mater 2024;413:134805.
[31] Kharrazi H, Ahmadi B, Shekarchi M, Farhoudi N. A comprehensive study of the effects of re-curing on macro- and microstructure of zeolite incorporating concretes after exposure to high temperature. Mater Struct 2023;56:50.
[32] Akca AH, Özyurt N. Effects of re-curing on microstructure of concrete after high temperature exposure. Constr Build Mater 2018;168:431–41.
[33] Park SJ, Yim HJ, Kwak HG. Effects of post-fire curing conditions on the restoration of material properties of fire-damaged concrete. Constr Build Mater 2015;99:90–8.
[34] Henry M, Darma IS, Sugiyama T. Analysis of the effect of heating and re-curing on the microstructure of high-strength concrete using X-ray CT. Constr Build Mater 2014;67:37–46.
[35] Liu L. Fire performance of high strength concrete materials and structural concrete. United States – Florida: Florida Atlantic University; 2009. p. 229.
[36] Alonso C, Fernandez L. Dehydration and rehydration processes of cement paste exposed to high temperature environments. J Mater Sci 2004;39:3015–24.
[37] Wang GM, Zhang C, Zhang B, Li Q, Shui ZH. Study on the high-temperature behavior and rehydration characteristics of hardened cement paste. Fire Mater 2015;39:741–50.
[38] Serpell R, Lopez M. Reactivated cementitious materials from hydrated cement paste wastes. Cem Concr Compos 2013;39:104–14.
[39] Qian YF, Yang DY, Liu M, Guo ZR, Xiao ZL, Ma ZM. Performance recovery of high-temperature damaged ultra-high-performance concrete under different curing environments. Dev Built Environ 2023;16:100274.
[40] Demir U, Goksu C, Binbir E, Ilki A. Impact of time after fire on post-fire seismic behavior of RC columns. Structures 2020;26:537–48.
[41] Li Y, Wang H, Lou H. Strength recovery of thermally damaged high-performance concrete during recuring. Materials 2024;17:3531.
[42] Li Y, Wang H, Shi C, Zou D, Zhou A, Liu T. Effect of post-fire lime-saturated water and water-CO_2 cyclic curing on strength recovery of thermally damaged high-performance concrete with different silica contents. Cem Concr Res 2023;164:107050.
[43] Ming X, Cao ML. Development of eco-efficient cementitious composites with high fire resistance and self-healing abilities - a review. Resour Conserv Recycl 2020;162:105017.
[44] Shui ZH, Xuan DX, Chen W, Yu R, Zhang R. Cementitious characteristics of hydrated cement paste subjected to various dehydration temperatures. Constr Build Mater 2009;23:531–7.
[45] Khaled A, Safhi AE, Soliman AM. Post-fire curing and autogenous self-healing in alkali-activated slag: microstructures and healing mechanisms. Constr Build Mater 2024;428:136334.
[46] Shui ZH, Xuan DX, Wan HW, Cao BB. Rehydration reactivity of recycled mortar from concrete waste experienced to thermal treatment. Constr Build Mater 2008;22:1723–9.

[47] Li L, Shi L, Wang QY, Liu YJ, Dong JF, Zhang H, et al. A review on the recovery of fire-damaged concrete with post-fire-curing. Constr Build Mater 2020;237:117564.
[48] Mindeguia J-C, Pimienta P, Noumowé A, Kanema M. Temperature, pore pressure and mass variation of concrete subjected to high temperature — Experimental and numerical discussion on spalling risk. Cem Concr Res 2010;40:477–87.
[49] Weidenfeller B, Höfer M, Schilling FR. Thermal conductivity, thermal diffusivity, and specific heat capacity of particle filled polypropylene. Compos Part A Appl Sci Manuf 2004;35:423–9.
[50] Weidenfeller B, Höfer M, Schilling F. Thermal and electrical properties of magnetite filled polymers. Compos Part A Appl Sci Manuf 2002;33:1041–53.
[51] Xing Z, Beaucour A-L, Hebert R, Noumowe A, Ledesert B. Aggregate's influence on thermophysical concrete properties at elevated temperature. Constr Build Mater 2015;95:18–28.
[52] Liu TJ, Wang HD, Zou DJ, Long X, Miah MJ, Li Y. Strength recovery of thermally damaged high-performance concrete subjected to post-fire carbonation curing. Cem Concr Compos 2023;143:105273.
[53] Wang HD, Lyu H, Liu TJ, Li Y, Tan KH. Effect of post-fire curing on compressive strength of ultra-high performance concrete and mortar. Constr Build Mater 2022;346:128447.
[54] London, UK: Britsh Standards Institution; 2006. p. 72–6.
[55] Heap MJ, LavallÉe Y, Laumann A, Hess KU, Meredith PG, Dingwell DB, et al. The influence of thermal-stressing (up to 1000 °C) on the physical, mechanical, and chemical properties of siliceous-aggregate, high-strength concrete. Constr Build Mater 2013;42:248–65.
[56] Andrade MSA, Ribeiro JCL, Oliveira DS d, Pedroti LG, Santos CFR. Experimental evaluation of concrete-reinforcement bond: bond failure mechanisms after exposure to elevated temperatures. Eng Struct 2024;311:118148.
[57] Liu C, Zhao K, Liu L, Yan L, Miao J. Bond strength of steel rebar and concrete after different cooling methods: experimental study and theoretical modeling. Constr Build Mater 2025;497:143851.
[58] Wang W, Dong Y. Temperature distribution of reinforced concrete T-shaped beam with slabs under (after) three-side fire exposure. J Cent South Univ Sci Technol 2015;46:684–93.
[59] Gao WY, Dai JG, Teng JG. Simple method for predicting temperatures in reinforced concrete beams exposed to a standard fire. Adv Struct Eng 2014;17:573–89.
[60] Li FB, Hu WB, Wu YP. Temperature field simulation and analysis of the frame column under fire based on ABAQUS. 4th International Conference on Technology of Architecture and Structure (ICTAS 2011). Xian, PEOPLES R CHINA: Xian Univ Architecture & Technol; 2011.
[61] Zha XX. Three-dimensional non-linear analysis of reinforced concrete members in fire. Build Environ 2003;38:297–307.
[62] Zha X, Zhong S. Calculation of temperature distributions in steel, concrete and composite members under different fires. J Harbin Univ Archit Eng 2002;35:16–20.
[63] Tao Z, Yu Q. Residual bond strength in steel reinforced concrete columns after fire exposure. Fire Saf J 2012;53:19–27.
[64] Abd.El.Aleem S, Heikal M, Morsi WM. Hydration characteristic, thermal expansion and microstructure of cement containing nano-silica. Constr Build Mater 2014;59:151–60.
[65] Radkovský F, Gawronová M, Merta V, Lichý P, Kroupová I, Nguyenová I, et al. Effect of the composition of hybrid sands on the change in thermal expansion. Materials 2022;15:6180.
[66] Kodur V, Khaliq W. Effect of temperature on thermal properties of different types of high-strength concrete. J Mater Civ Eng 2011;23:793–801.
[67] Khaliq W, Kodur V. Thermal and mechanical properties of fiber reinforced high performance self-consolidating concrete at elevated temperatures. Cem Concr Res 2011;41:1112–22.
[68] Zhou C, Shu X, Huang B. Predicting concrete coefficient of thermal expansion with an improved micromechanical model. Constr Build Mater 2014;68:10–6.
[69] Zhang Y, Ju JW, Zhu HH, Guo QH, Yan ZG. Micromechanics based multi-level model for predicting the coefficients of thermal expansion of hybrid fiber reinforced concrete. Constr Build Mater 2018;190:948–63.
[70] Ma QM, Guo RX, Zhao ZM, Lin ZW, He KC. Mechanical properties of concrete at high temperature-a review. Constr Build Mater 2015;93:371–83.
[71] Georgali B, Tsakiridis PE. Microstructure of fire-damaged concrete. A case study. Cem Concr Compos 2005;27:255–9.
[72] Abdelmelek N, S. Alimrani N, Krelias N, Lublóy É. Effect of elevated temperatures on microstructure of high strength concrete based-metakaolin. J King Saud Univ Eng Sci 2021:7–9.
[73] Wang H. Effect of recuring on recovery of mechanical properties of thermally damaged high performance concrete. Harbin: Harbin Institute of Technology; 2021. p. 60–4.
[74] Piasta J. Heat deformations of cement paste phases and the microstructure of cement paste. Matériaux Et Constr 1984;17:415–20.
[75] Zhang Q, Ye G, Koenders E. Investigation of the structure of heated Portland cement paste by using various techniques. Constr Build Mater 2013;38:1040–50.
[76] Yim HJ, Park SJ, Jun YB. Physicochemical and mechanical changes of thermally damaged cement pastes and concrete for recuring conditions. Cem Concr Res 2019;125:105831.
[77] Huang H, Ye G, Damidot D. Effect of blast furnace slag on self-healing of microcracks in cementitious materials. Cem Concr Res 2014;60:68–82.
[78] Pan X, Shi C, Hu X, Ou Z. Effects of CO2 surface treatment on strength and permeability of one-day-aged cement mortar. Constr Build Mater 2017;154:1087–95.
[79] Cizer Ö, Van Balen K, Elsen J, Van Gemert D. Real-time investigation of reaction rate and mineral phase modifications of lime carbonation. Constr Build Mater 2012;35:741–51.
[80] Poon CS, Azhar S, Anson M, Wong YL. Strength and durability recovery of fire-damaged concrete after post-fire-curing. Cem Concr Res 2001;31:1307–18.
[81] Hager I, Tracz T, Choinska M, Mróz K. Effect of cement type on the mechanical behavior and permeability of concrete subjected to high temperatures. Materials 2019;12:3021.
[82] Park SJ, Yim HJ. Evaluation of residual mechanical properties of concrete after exposure to high temperatures using impact resonance method. Constr Build Mater 2016;129:89–97.
[83] Peters S, Vu G, Meschke G. A multiscale model for predicting the Young's modulus and the thermal-expansion coefficient of concrete at high temperatures. Constr Build Mater 2025;479:141259.
[84] Dong CX, Kwan AKH, Ho JCM. A constitutive model for predicting the lateral strain of confined concrete. Eng Struct 2015;91:155–66.
[85] Suh H, Jee H, Kim J, Kitagaki R, Ohki S, Woo S, et al. Influences of rehydration conditions on the mechanical and atomic structural recovery characteristics of Portland cement paste exposed to elevated temperatures. Constr Build Mater 2020;235:117453.
[86] Nalon GH, Ribeiro JCL, DE END, ARAÚJO, Pedroti LG, de Carvalho JMF, et al. Effects of post-fire curing on the mechanical properties of cement composites containing carbon black nanoparticles and multi-walled carbon nanotubes. Constr Build Mater 2021;310:125118.
[87] Li Q, Xia H, Yuan G, Shu Q. Experimental study on the free expansion deformation of concrete during the cooling process after being heated to high temperature. Constr Build Mater 2022;337:127617.
[88] Pessiki S, Pieroni A. Axial load behavior of large-scale spirally-reinforced high-strength concrete columns. Acids Struct J 1997;94:304–14.
[89] Choi W-C, Yun H-D. Compressive behavior of reinforced concrete columns with recycled aggregate under uniaxial loading. Eng Struct 2012;41:285–93.
[90] Li D. Research on size effect of concrete and RC columns. Beijing: Beijing University of Technology; 2017. p. 158–61.
[91] Sturm AB, Visintin P. Local bond slip behavior of steel reinforcing bars embedded in ultra high performance fibre reinforced concrete. Struct Concr 2019;20:108–22.
[92] Zhang T, Yin Y, Gong Y, Wang L. Mechanical properties of jute fiber-reinforced high-strength concrete. Struct Concr 2020;21:703–12.
[93] Yu J, Yao YL, Wang KZ, Zhou J, Zhou WD, Zhang C, et al. Experimental investigation of effects of multi-fissures on brittleness of ordinary Portland cement concrete and rubberized concrete. Eng Fract Mech 2024;306.
[94] Rawat S, Lee CK, Fanna DJ, George L, Zhang YX. Mechanism and effect of Re-curing on strength recovery of fire-damaged high strength engineered cementitious composite. Constr Build Mater 2025;461:139920.
[95] Ji J, Yu D, Jiang L, Xu Z, Liu Y, Zhang S. Effect of post-fire curing on the compressive properties of fire-damaged ultra-high toughness cementitious composites. J Test Eval 2019;47:140–52.
[96] Neves IC, Rodrigues JPC, Loureiro AD. Mechanical properties of reinforcing and prestressing steels after heating. J Mater Civ Eng 1996;8:189–94.
[97] Kodur VKR, Cheng FP, Wang TC, Sultan MA. Effect of strength and fiber reinforcement on fire resistance of high-strength concrete columns. J Struct Eng ASCE 2003;129:253–9.
[98] Elsayed M, Ali M, El-Azim AA. Residual strength of ultrahigh-performance hybrid fibre-reinforced concrete columns subjected to high temperatures. Constr Build Mater 2024;411:134305.
[99] Mao WJ, Zhou K, Wang WD. Investigation on fire resistance of steel-reinforced concrete-filled steel tubular columns subjected to non-uniform fire. Eng Struct 2023;280.
[100] Abd elsalam MM, Agamy MH, Genidi MMM, Salem M. Fire resistance of square concrete columns reinforced with GFRP bars, experimental and numerical investigation. Eng Struct 2024;305:117732.